Metamagnetic transitions and magnetoelectric responses in the chiral polar helimagnet Ni_2InSbO_6

Y. Araki,[1] T. Sato,[1] Y. Fujima,[1] N. Abe,[1] M. Tokunaga,[2] S. Kimura,[3] D. Morikawa,[4] V. Ukleev,[4] Y. Yamasaki,[4,5] C. Tabata,[6] H. Nakao,[7] Y. Murakami,[7] H. Sagayama,[7] K. Ohishi,[8] Y. Tokunaga,[1] and T. Arima[1,4]

[1]*Department of Advanced Materials Science, University of Tokyo, Kashiwa 277-8561, Japan*
[2]*Institute for Solid State Physics, University of Tokyo, Kashiwa 277-8581, Japan*
[3]*Institute for Materials Research, Tohoku University, Sendai 980-8577, Japan*
[4]*RIKEN Center for Emergent Matter Science (CEMS), Wako 351-0198, Japan*
[5]*Research and Service Division of Materials Data and Integrated System (MaDIS), National Institute for Materials Science (NIMS), Tsukuba 305-0047, Japan*
[6]*Institute of Materials Structure Science, High Energy Accelerator Research Organization, Tsukuba 305-0801, Japan*
[7]*Condensed Matter Research Center and Photon Factory, Institute of Materials Structure Science High Energy Accelerator Research Organization, Tsukuba 305-0801, Japan*
[8]*Neutron Science and Technology Center, Comprehensive Research Organization for Science and Society (CROSS),Tokai 319-1106, Japan*

(Received 3 December 2019; revised 11 June 2020; accepted 21 July 2020; published 5 August 2020)

In this study, the magnetic field effect was investigated on the magnetic and electric properties of a chiral-polar-ordered corundum, Ni_2InSbO_6. Single-crystal soft x-ray and neutron diffraction measurements were used to verify the magnetic modulations with long wavelengths. The modulation direction tends to align along the magnetic field when it is applied perpendicular to the polar axis, suggesting that the nearly proper-screw-type helicoid should be formed below 77 K owing to the dominant activation of chirality-induced uniform Dzyaloshinskii-Moriya interactions despite the existence of both chirality and polarity. When a high magnetic field is applied perpendicular to the polar axis, a helix-to-canted antiferromagnetic transition is observed through the intermediate soliton lattice type state. In contrast, a magnetic field applied along the polar axis induces a first-order metamagnetic transition. These metamagnetic transitions accompany a change in the electric polarization along the polar axis.

DOI: 10.1103/PhysRevB.102.054409

I. INTRODUCTION

Noncentrosymmetric magnets often host noncollinear or noncoplanar spin arrangements, such as magnetic helices, solitons, and skyrmions [1,2] owing to the presence of the uniform antisymmetric exchange interaction $\boldsymbol{D} \cdot (\boldsymbol{S}_i \times \boldsymbol{S}_j)$ between the neighboring spins $\boldsymbol{S}_i$ and $\boldsymbol{S}_j$. The Dzyaloshinskii-Moriya (DM) vector $\boldsymbol{D}$ is parallel to the bond direction in chiral magnets. As a result, magnetic helix, cone, Bloch-type-skyrmion lattice, and chiral soliton lattice have been reported in B20-type compounds [3], β-Mn-type Co-Zn-Mn alloys [4], and Cu_2OSeO_3 [5] with chiral cubic structures. Néel-type-skyrmion lattice is observed in polar magnets, such as GaV_4S_8 [6], GaV_4Se_8 [7], and $VOSe_2O_5$ [8], because $\boldsymbol{D}$ is perpendicular to the bond direction and polar axis. Furthermore, antiskyrmions appear in magnets with D_{2d}-symmetry [9]. The skyrmion lattices in insulating materials, such as Cu_2OSeO_3 and GaV_4S_8, have been found to accompany magnetoelectric (ME) coupling [10,11]. The cross-correlation response attracts interest in terms of the electric field control of magnetic structures; particularly, topological magnetic objects.

To explore a colossal ME response with specific spin ordering, magnetic oxides of Ni_3TeO_6-type chiral-polar-ordered corundum structure with a space group $R3$ may be good candidates [12]. Ni_3TeO_6 undergoes an antiferromagnetic transition at 52 K [13]. Below the Néel temperature, the material shows colossal ME effects across two-step spin-flop transitions [14–16]. This study focuses on isostructural Ni_2InSbO_6, which is obtained by substituting Sb^{5+} and In^{3+} for Te^{6+} and one third of Ni^{2+}, respectively. The lattice parameters are $a = 5.2168$ Å and $c = 14.0166$ Å in the hexagonal notation (we use the hexagonal notation in this study). While the Ni moments in Ni_3TeO_6 are collinearly arranged in the antiferromagnetic phase, Ni_2InSbO_6 hosts an incommensurate helimagnetic modulation with a propagation vector $\boldsymbol{q} = 0.029\boldsymbol{b}^*$ below $T_C = 76$ K according to the powder neutron diffraction [17]. The typical wavelength of a helimagnetic order in the centrosymmetric frustrated magnets is shorter than 10 nm; for example, 2 nm in $TbMnO_3$ [18,19] and 7 nm in $NiBr_2$ [20–22]. When the antisymmetric exchange induces the helimagnetic order, the wavelength tends to be longer (1–100 nm), such as in Cu_2OSeO_3 (62 nm [5,23]). The helimagnetic period of 15.6 nm in Ni_2InSbO_6 corresponds to 30 unit cells, thereby suggesting that the antisymmetric exchange, termed as DM interaction, should be essential for the helimagnetic order. The helimagnetically ordered Ni planes are stacked along the c axis in an out-of-phase manner, as that in $Fe_3PO_4O_3$ [24,25]. Owing to the noncentrosymmetric nature of the underlying crystal structure with both chirality and polarity, Ni_2InSbO_6 can exhibit a unique magnetic property and fascinating ME responses. The DM interaction, activated in a C_3-symmetry magnet, which possesses both chirality and polarity, can work differently from that in either

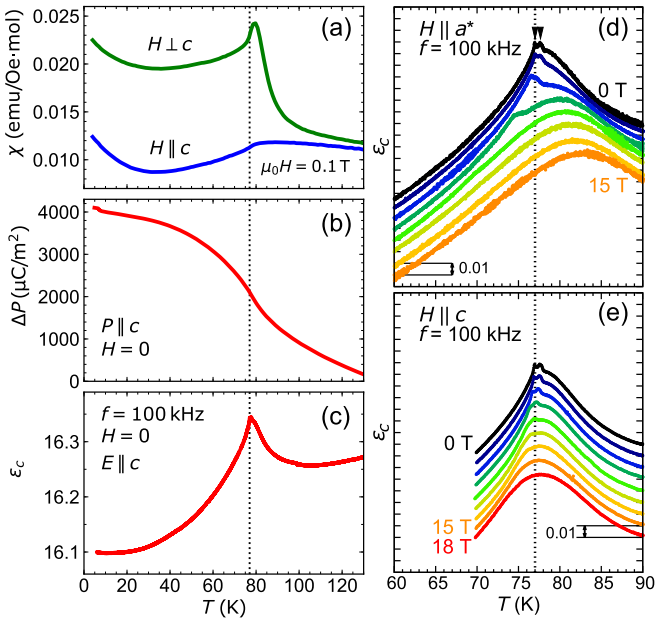

FIG. 1. Temperature dependence of (a) magnetic susceptibility χ, (b) change in electric polarization ΔP, and (c) electric permittivity ε_c along the c axis at a frequency of 100 kHz. (d),(e) Temperature dependence of ε_c in magnetic fields of 0, 2, 4, 6, 8, 10, 12, and 15 T for (d) $\boldsymbol{H} \parallel \boldsymbol{a}^*$ and (e) $\boldsymbol{H} \parallel \boldsymbol{c}$. 18-T data are also added for $\boldsymbol{H} \parallel \boldsymbol{c}$. Data are vertically offset for clarity. Dotted lines in (a)–(e) show a magnetic transition at $T_{C1} = 77$ K. Two black triangles are located at T_{C1} and $T_{C2} = 78$ K.

polar or chiral magnets [26]. In addition, Ni_2InSbO_6 exhibits antiferromagnetic coupling along the c axis. Noncentrosymmetric antiferromagnets have garnered significant interest from the viewpoint of nontrivial antiferromagnetic spin texture, such as antiferromagnetic solitons [27–34] and antiferromagnetic skyrmions [35–38]. Ni_2InSbO_6 is a rare antiferromagnet belonging to the C_3 point group that hosts noncollinear spiral spin ordering.

Here, we study the physical properties of Ni_2InSbO_6 using single crystals. Because a spin helix exhibits an anisotropic response to an external field, generally, experimental research using single crystalline samples is required to clarify the multiferroic property of the unique spin spiral order [39]. We found that large pyroelectricity is induced by the "nearly proper-screw" type helimagnetic order that is accompanied with a sinusoidally modulated canted component along the $\boldsymbol{q}$ direction. Furthermore, metamagnetic transitions are observed by measuring the magnetization, electric polarization, and electric permittivity in high magnetic fields.

II. EXPERIMENTS

Single crystals of Ni_2InSbO_6 were grown by the chemical vapor transport method using $PtCl_2$ as the transport agent [40]. The c plane was easily grown, resulting in plate-shaped crystals. The typical dimensions of obtained crystals included an area and thickness of 1–3 mm^2 and 500 μm, respectively. Polarized light microscopy clarified that they had chiral twins, as reported in Ref. [41]. Since it was reported that isostructural Ni_3TeO_6 hosts the composite domain walls of chirality and polarity [42], the electric polarization along the c axis was measured on a homochiral domain with an area of 0.74 mm^2, by integrating the displacement current, measured using an electrometer (6517A, Keithley). The dielectric constants were measured using an LCR meter (E4980A, Agilent). The magnetization was measured by a superconducting quantum interference device magnetometer (MPMS-XL, Quantum Design). High magnetic field measurements for the magnetization and electric polarization were performed using a pulse magnet at the Institute for Solid State Physics, the University of Tokyo. Dielectric constant measurements in steady high magnetic fields were performed at the High Field Laboratory for Superconducting Materials, Institute for Materials Research, Tohoku University. Small-angle soft x-ray scattering (SAXS) measurements at the Ni L_3 absorption edge were performed on BL-16A and 19B, Photon Factory, KEK, Japan. The experimental setup for the SAXS measurements is schematically shown in Fig. 2(a) (see Refs. [43,44] for details). A plate of Ni_2InSbO_6 crystal with a thickness of approximately 300 nm was fabricated using a focused ion beam thinning method. The thin-plate sample was put on a Si_3N_4 membrane covered with a gold film with a pin hole (diameter = 5 μm), as depicted in Fig. 2(b). We used left-handed circularly polarized and unpolarized x rays at BL-16A and BL-19B, respectively. A soft x ray, 853-eV (Ni L_3 edge), was irradiated on the sample and the scattered x ray around the direct beam was recorded by a charge-coupled detector camera with 2048 × 2048 pixels. A time-of-flight neutron scattering measurement was performed on BL15 in MLF, J-PARC, Japan [45]. Three crystals were aligned on an Al plate and cooled in a ^{4}He closed-cycle refrigerator. Small- and wide-angle neutron scattering were recorded by position sensitive detectors.

III. FUNDAMENTAL PHYSICAL PROPERTIES

Figure 1 shows the fundamental physical properties of Ni_2InSbO_6 as functions of the temperature T. Magnetic susceptibility exhibits an anomaly at $T_{C1} = 77$ K. The temperature is approximately consistent with the previously reported magnetic transition temperature [17]. The Weiss temperature θ_W is estimated to be −207 and −188 K considering the susceptibility data above 150 K (not shown) for magnetic fields $\boldsymbol{H} \perp \boldsymbol{c}$ and $\boldsymbol{H} \parallel \boldsymbol{c}$, respectively. The frustration parameter $|\theta_W/T_{C1}|$ is smaller than 3, implying that the DM interaction should be the dominant origin of the helimagnetic order instead of magnetic frustration; however, the effect of magnetic frustration cannot be excluded. Figure 1(b) depicts a steep change in electric polarization ΔP around T_{C1}, superposed on a large pyroelectricity owing to the polar nature of the crystal. A change of approximately 2000 $\mu C/m^2$ was observed in the electric polarization between T_{C1} and the lowest temperature. This value is almost comparable to Ni_3TeO_6[14] and larger than the typical value of the order of $\mu C/m^2$ in other multiferroic materials [46].

Figures 1(d) and 1(e) display the temperature dependence of the electric permittivity ε_c along the c axis around T_{C1} in various magnetic fields. A double peak structure is observed around T_{C1} in zero field, as indicated by black triangles, which suggests two-step successive phase transitions at $T_{C1} = 77$ K and $T_{C2} = 78$ K. An in-plane magnetic field $\boldsymbol{H} \parallel \boldsymbol{a}^*$ shifts T_{C1}

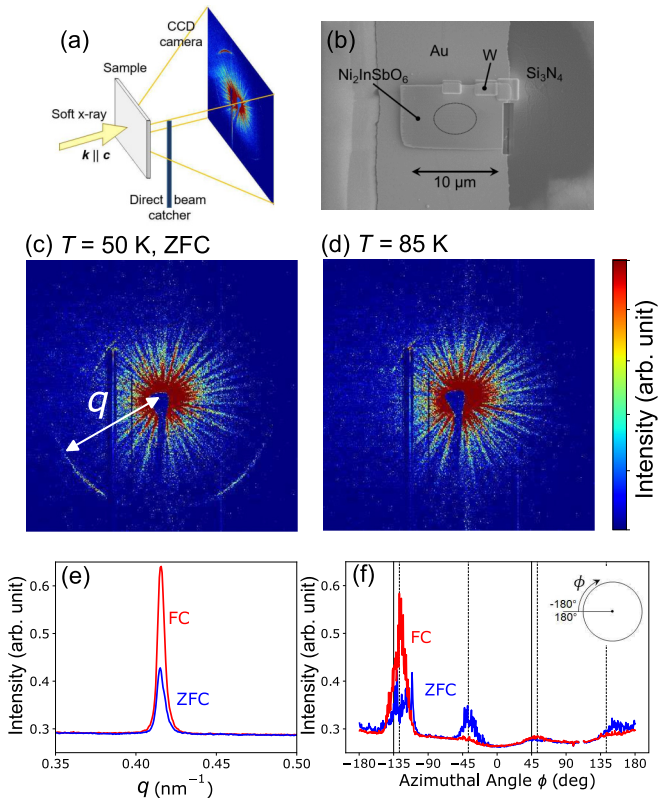

FIG. 2. Small-angle resonant soft x ray scattering of Ni_2InSbO_6 for the incident x ray propagating parallel to the c axis. (a) Schematic of experimental setup for SAXS measurements. (b) Thin plate fabricated by a focused ion beam process on a gold-coated Si_3N_4 membrane. The dotted line indicates the position of a circle-shaped pinhole. (c),(d) Diffraction patterns in zero magnetic field at (c) 50 K (below T_{C1}) and (d) 85 K (above T_{C1}). (e) Intensity profiles of x ray scattering along the radial direction at 50 K. The intensity is obtained by integration in the range of $-142.5^\circ < \phi < -112.5^\circ$. ZFC and FC denote zero-magnetic-field cooling and field cooling in a magnetic field of 0.4 T along $\phi = -135^\circ$, respectively. (f) Intensity profiles of x ray scattering along the azimuthal angle ϕ at 50 K for $0.406\ \text{nm}^{-1} < |\boldsymbol{q}| < 0.423\ \text{nm}^{-1}$. The inset states the definition of ϕ. Two solid vertical lines show $\phi = -135^\circ$ and 45°, which are parallel to the cooling-magnetic-field direction.

to lower temperatures and makes it less prominent. The higher temperature peak at T_{C2} becomes smaller as the magnetic field increases, and it merges with the lower temperature anomaly at T_{C1}. This change accompanies the emergence of another anomaly at approximately $T_{C3} = 80$ K at 6 T, which gradually shifts to higher temperatures as the magnetic field increases. In contrast, a magnetic field along the c axis only broadens the peaks at T_{C1} and T_{C2}, as shown in Fig. 1(e).

IV. SMALL-ANGLE RESONANT SOFT X-RAY MAGNETIC SCATTERING

A SAXS measurement in resonance with the Ni L_3 absorption edge was performed with the incident x ray propagating in the c direction. A ringlike profile in the c plane is observed at 50 K (below T_{C1}) after zero-field cooling (ZFC), as shown in Fig. 2(c). Note that the shadow of a direct beam catcher is observed at the center of the image. The diffraction disappears at 85 K (above T_{C1}), as shown in Fig. 2(d), suggesting its magnetic origin. Figure 2(e) shows the intensity profiles along $|\boldsymbol{q}|$ at an azimuthal angle of $\phi = -127.5^\circ$ after zero-field cooling and field cooling. By performing pseudo-Voigt fitting on the field-cooling profile along radial direction, the position and half-width at half-maximum of the superlattice peak are estimated to be 4.15×10^{-1} nm^{-1} and 5.73×10^{-3} nm^{-1}, respectively. The sharp peak profile indicates the well-defined period $\lambda = 15 \pm 1$ nm of the helimagnetic order, which is in accordance with a previous report [17]. A fourfold like broad intensity profile is observed in the azimuthal angle dependence of the zero-field cooling pattern, as shown in Figs. 2(c) and 2(f); however the c axis is the threefold axis. This discrepancy may arise from some strain caused by the difference in the thermal expansion between the sample plate and Si_3N_4 membrane, as shown in Fig. 2(b). We also confirmed that the modulation direction can be controlled via magnetic-field cooling. Figure 2(f) compares the intensity profile along the azimuthal angle ϕ in zero magnetic field at 50 K after zero magnetic field cooling with that after the sample was cooled from above T_{C1} in a magnetic field, $\mu_0 H = 0.4$ T, in the direction of $\phi = 45^\circ$. The scattering intensities around $\phi \simeq -135^\circ$ and 45°, which are located along the field direction, increase after the field-cooling procedure, while those around $\phi \simeq -45^\circ$ and 135° decrease. Because the propagation direction of the helix tends to rotate along a magnetic field so that the spiral plane becomes normal to the magnetic-field direction to maximize the Zeeman-energy gain, the observed field-cooling effect implies that the helimagnetic order should be nearly of proper-screw type. The chiral component of the DM interaction, i.e., the DM vector component parallel to the bond, should be dominant over the polar one (DM vector component perpendicular to the bond).

V. NEUTRON DIFFRACTION

The effect of a magnetic field on the helicoid was also confirmed by neutron scattering. Figure 3 illustrates a contour map of the intensity of neutron diffraction on the two-dimensional reciprocal $(hk3)$ plane. Ringlike scattering is observed around the (003) reflection at 60 K (below T_{C1}) and it disappears at 80 K (above T_{C1}). The ring shape indicates that the direction of the modulation vector $\boldsymbol{q}$ of helimagnetic order in the bulk sample should be distributed isotropically in the c plane, suggesting weak in-plane magnetic anisotropy as observed in some other DM helimagnets [6,8,47,48]. The period of magnetic modulation is estimated to be approximately 15.7 nm, which is consistent with a previous report [17] as well as the present SAXS result. The application of a magnetic field of 6 T along the a^* axis at 60 K concentrates the intensity of the magnetic diffraction along the field [Fig. 3(b)], which is again in accordance with the SAXS result. Figure 3(d) shows the temperature dependence of (003) and satellite intensities at 6 T. The (003) intensity reaches the maximum just below T_{C1}, and decreases above 80 K. In contrast, the satellite intensity decreases with an increase in the temperature, and it is almost the same as the background level above 80 K. These behaviors approximately correspond to the anomalies

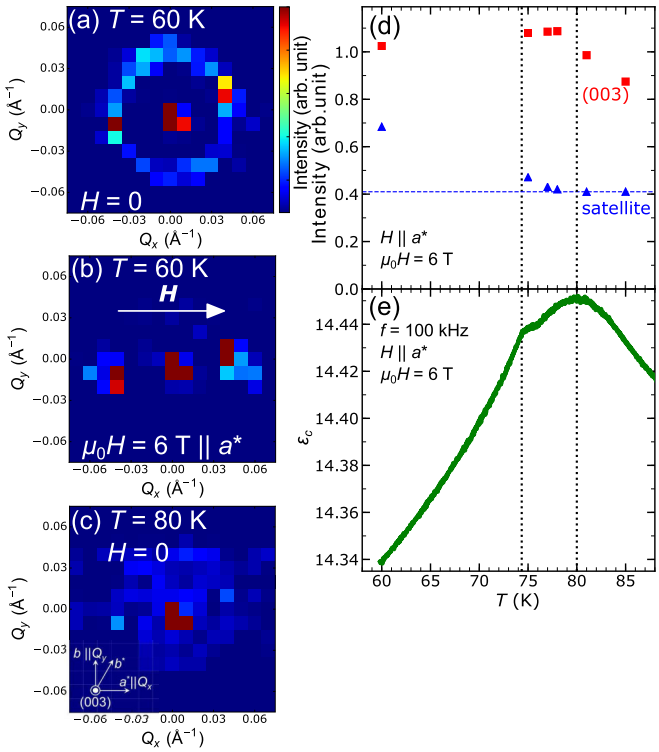

FIG. 3. Neutron scattering patterns in the ($hk3$) plane. Q_x and Q_y are along the a^* and b axes, respectively. The inset in (c) shows the reciprocal space vectors in the experimental setup. (a) Scattering pattern at 0 T and 60 K. (b) Scattering pattern at $\mu_0 H = 6$ T and 60 K. The magnetic field of 6 T was first applied along the a^* axis, and then the sample was cooled to the ordered phase. (c) Scattering pattern at 80 K (above T_{C1}). (d) Temperature dependences of the intensity of (003) (red squares) and satellite diffractions (blue triangles). A blue horizontal broken line shows the background level of satellite diffractions determined by the data for 85 K (far above T_{C1}). (e) Temperature dependence of the electric permittivity in a magnetic field $\mu_0 H$ of 6 T along the a^* axis. Vertical dotted lines act as a visual guide.

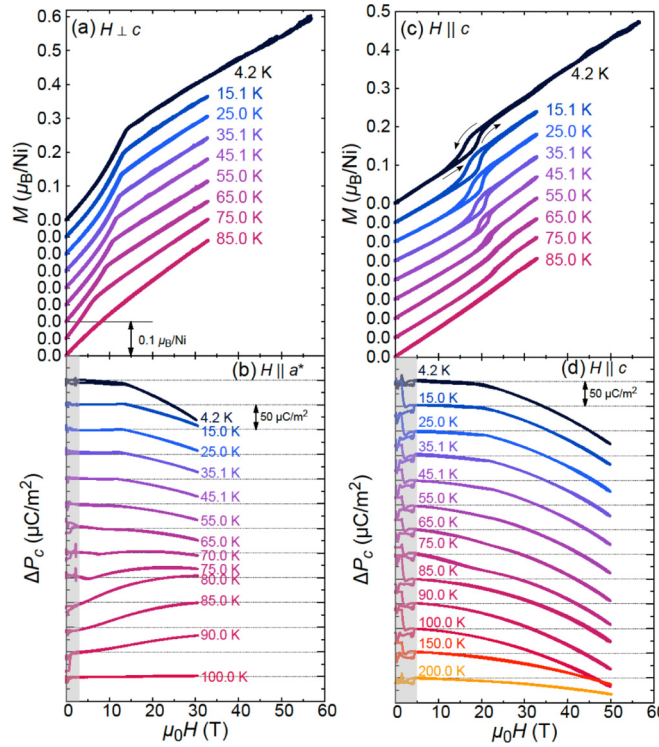

FIG. 4. (a),(c) Magnetic-field dependence of the magnetization M at various temperatures in the (a) $\boldsymbol{H} \perp \boldsymbol{c}$ and (c) $\boldsymbol{H} \parallel \boldsymbol{c}$ configurations. (b),(d) Magnetic-field dependence of the change in electric polarization ΔP_c along the c axis at various temperatures in (b) $\boldsymbol{H} \parallel \boldsymbol{a}^*$ and (d) $\boldsymbol{H} \parallel \boldsymbol{c}$ configurations. Anomalies in the shaded area at low fields are due to electric noise at the ignition of the pulse magnet. The M-H and P-H curves in each panel are vertically offset for clarity.

of dielectric constant in a magnetic field of 6 T, as depicted in Fig. 3(e). The small difference between the onset of the magnetic satellite and the anomaly in the dielectric constant may originate from possible errors in the monitoring temperature. The system may first undergo a magnetic transition to the commensurate layered antiferromagnetic phase upon cooling, and then successively enter the helical phase with a long-wavelength modulation below 74 K.

VI. PULSE MAGNET MEASUREMENT

Figure 4 shows magnetic-field dependences of the magnetization M and the change in electric polarization ΔP_c at various temperatures measured using a pulse magnet. For $\boldsymbol{H} \perp \boldsymbol{c}$, the M-H curves below T_{C1} have a clear anomaly, as shown in Fig. 4(a), which can be ascribed to a metamagnetic transition. The transition field H_c is approximately 14 T at 4.2 K; it decreases monotonically with a rise in the temperature, and disappears above T_{C1}, as shown in the curve at 85 K. The magnetization below H_c is superlinear to the field, which could be featured by soliton lattice formation [49–51], as discussed later. The magnetization in a higher-field phase below T_{C1} is linear to the magnetic field, and the extrapolation to $\mu_0 H = 0$ T remains nonzero (0.17 μ_B/Ni at 4.2 K), suggesting that the higher-field phase should essentially have a spontaneous magnetization component. The extrapolated value decreases monotonically with an increase in the temperature. When a magnetic field is applied along the c axis ($\boldsymbol{H} \parallel \boldsymbol{c}$), however, a metamagnetic transition with a hysteresis loop is observed, as shown in Fig. 4(c). The transition field increases and the hysteresis loop becomes smaller with a rise in temperature. Similar to the case of $\boldsymbol{H} \perp \boldsymbol{c}$ configuration, the field-induced magnetic transition disappears above T_{C1}.

As shown in Figs. 4(b) and 4(d), the change in electric polarization shows an anomaly at the metamagnetic transition. The electric polarization below T_{C1} is almost insensitive to the magnetic field perpendicular to the c axis in the low-field phase; however, in the high-field phase, it shows parabolic dependence on the magnetic field. Around T_{C1}, the sign of the ME coefficient is reversed, and the parabolic dependence disappears. The value of ΔP_c at each temperature in the high-field phase is on the order of 10 μC/m^2, which is significantly smaller than the pyroelectricity at zero field. ME coupling remains even above T_{C1}. The electric polarization exhibits quadratic dependence on the magnetic field for $\boldsymbol{H} \parallel \boldsymbol{c}$ in both low- and high-field phases. The typical value is comparable

with that in the $\boldsymbol{H} \perp \boldsymbol{c}$ configuration. The quadratic ME effect is observed up to 200 K. The sign of the ME effect does not change in the whole temperature range, in contrast to the case of $\boldsymbol{H} \perp \boldsymbol{c}$.

VII. MAGNETIC PHASE DIAGRAM

Based on the dielectric constant, electric polarization, and magnetization data, as well as SAXS and neutron diffraction profiles, we propose the magnetic phase diagrams of Ni_2InSbO_6, as shown in Figs. 5(a) and 5(b). The gray and light red areas indicate the helical and paramagnetic phases, respectively, as previously reported in Ref. [17]. A small green pocket "A" between the helical and paramagnetic phases is revealed by the dielectric property. The nature of this phase is still unknown because SAXS and neutron diffraction intensities are too weak to be analyzed. The high-field phases for $\boldsymbol{H} \perp \boldsymbol{c}$ (light blue area) and $\boldsymbol{H} \parallel \boldsymbol{c}$ are determined by the present high-field measurements. The magnetic structures of these phases are not settled yet.

VIII. DISCUSSIONS

We discuss the variations in the magnetic structure of Ni_2InSbO_6. As obeserved in SAXS and neutron measurements, the anisotropy of the $\boldsymbol{q}$ direction is significantly weak. Therefore, the helimagnetic order includes short-range helical domains with random $\boldsymbol{q}$ directions. The linear M-H behavior above H_c should be assigned to some noncollinear magnetic structure. Since the zero-field extrapolation is not zero, the canting is likely generated by the antisymmetric exchange. The long-wavelength helix with an in-plane propagation vector indicates that the in-plane magnetic order can be affected by external stimuli more than the antiferromagnetic stacking along the c axis. From a simple discussion based on the symmetry, the layered antiferromagnetic order should be weakly canted, if the moments lie in the plane. We hence speculate that the high-field phase is likely the canted antiferromagnetic phase, although we cannot exclude other possibilities. The low-field phase in the $\boldsymbol{H} \perp \boldsymbol{c}$ configuration below H_c is not likely assigned to the conical nor fan phase, which generally exhibit upward convex and discontinuous M-H curves, respectively [52–54]. The observed superlinear behavior in the M-H curve [Fig. 4(a)] suggests the soliton lattice phase owing to the modulation of the nearly proper-screw type helicoid [Fig. 5(c)]. The formation of the field-induced soliton phase is consistent with the assumption that the dominant origin of the helimagnetic order is the DM interaction instead of magnetic frustration. As shown in Fig. 3(b), the $\boldsymbol{q}$ direction is aligned nearly along the external field in Ni_2InSbO_6 below several tesla. On increasing the magnetic field, the helical structure is gradually modified in the $\boldsymbol{H} \parallel \boldsymbol{q}$ configuration. In a chiral ferromagnet with uniaxial $\boldsymbol{q}$, a chiral-soliton lattice can be formed in the $\boldsymbol{H} \perp \boldsymbol{q}$ configuration [49–51]. In contrast, the formation of solitons in a magnetic field is not straightforward in chiral antiferromagnets. Above a critical field H_c, the canted antiferromagnetic structure should appear, such as in the case in $BiFeO_3$ [55,56]. To explain the emergence of the soliton and canted antiferromagnetic phase in the $\boldsymbol{H} \perp \boldsymbol{c}$ configuration, we consider additional staggered DM interactions,

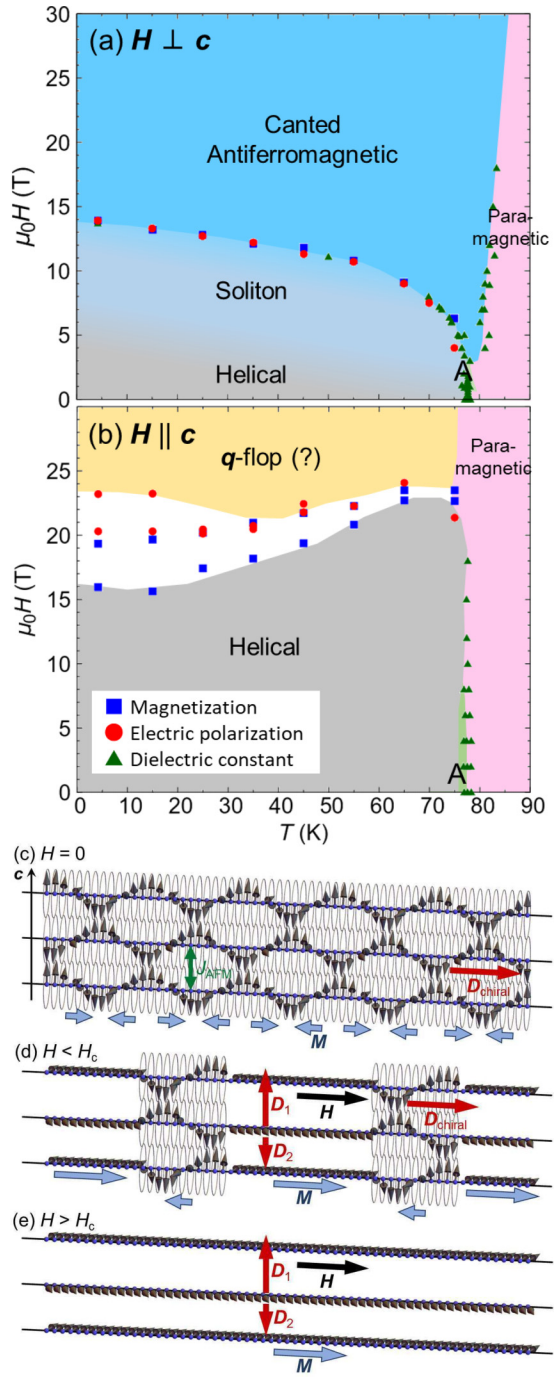

FIG. 5. Magnetic phase diagrams of Ni_2InSbO_6 proposed by macroscopic and quantum beam measurements in configurations (a)$\boldsymbol{H} \perp \boldsymbol{c}$ and (b)$\boldsymbol{H} \parallel \boldsymbol{c}$. The white area located between the blue and yellow areas in $\boldsymbol{H} \parallel \boldsymbol{c}$ configuration shows the hysteresis loop (upper and lower points are obtained in the field-increasing and -decreasing processes, respectively). (c)–(e) Schematic of the proposed magnetization process in $\boldsymbol{H} \perp \boldsymbol{c}$. For simplicity, polarity-induced uniform DM interaction is neglected. (c) Proper-screw helicoid at zero field. (d) Soliton lattice state induced by a moderate magnetic field below H_c. (e) Canted antiferromagnetic structure in a magnetic field higher than the critical field H_c.

because neither a chirality- nor polarity-induced uniform DM interaction can drive the spontaneous magnetization. In this system, crystallographically inequivalent Ni1 and Ni2

layers are alternately stacked along the c axis. In addition to the antiferromagnetic symmetric exchange between Ni moments on neighboring layers, the lack of an inversion center allows antisymmetric exchange interactions. The average of the DM vectors between a Ni1 moment and three adjacent Ni moments on the upper Ni2 layer ($\boldsymbol{D}_1$ in Fig. 5) should be different from that between a Ni1 moment and three adjacent Ni moments on the lower Ni2 layer ($\boldsymbol{D}_2$ in Fig. 5). The DM vectors tend to align the magnetic moments on the Ni1 and Ni2 layers noncollinearly if the Ni moments are in the c plane, while the antisymmetric exchange is inactive if the Ni moments are along the c axis. Therefore, when the Ni moments are arranged to form a layered antiferromagnetic structure, a uniform canted weak-ferromagnetic component can emerge in the c plane. This situation is expected above the critical field H_c, as shown in Fig. 5(e). Here, the weak ferromagnetic component is positioned along the $\boldsymbol{H}$ direction. When the magnetic field is reversed, the weak ferromagnetic moment flips, which should be accompanied with the reversal of the sublattice moment. At $H = 0$, however, the staggered DM vectors induce local weak ferromagnetic moments at positions where the Ni moments have c plane components on the proper-screw structure. These local weak ferromagnetic components are sinusoidally modulated along the $\boldsymbol{q}$ direction in the original proper-screw structure [Fig. 5(c)]. Hence, the application of a magnetic field in the c plane modifies the sinusoid (and thus the underlying proper-screw structure) so that the regions with a local weak ferromagnetic moment parallel (antiparallel) to the field expand (shrink) to acquire the Zeeman energy gain, resulting in the formation of the soliton structure, as shown in Fig. 5(d).

In contrast, the isothermal magnetization curve in the $\boldsymbol{H} \parallel \boldsymbol{c}$ configuration is almost linear below the critical field. Differences can occur between two magnetic field configurations irrespective of the stabilization of the local weak ferromagnetic component by the DM interaction. The nature of the observed field-induced magnetic transition in the $\boldsymbol{H} \parallel \boldsymbol{c}$ configuration is not evident at this stage. A magnetic cone with modulations along the c axis, such as those in Ni_3TeO_6 [57] and Co-doped Ni_2ScSbO_6 [58] is a possible magnetic order in a high external magnetic field along the c axis. Another possible scenario is the induction of a simple canted layered antiferromagnetic structure, similar to the case of $\boldsymbol{H} \perp \boldsymbol{c}$.

The temperature dependence of electric polarization is shown in Fig. 1(b). The proper-screw type helicoid drives a considerably large pyroelectricity. To consider the origin of the ME properties, we examine the inverse DM mechanism [59], exchange striction, and spin-direction dependent p-d hybridization [60]. The inverse DM effect cannot work effectively in a proper-screw helicoid. The electric polarization driven by the exchange striction mechanism ΔP_z^{ex} is expressed as

$$\Delta P_z^{\mathrm{ex}} = C\boldsymbol{S}_{\mathrm{Ni1}} \cdot \boldsymbol{S}_{\mathrm{Ni2}}. \tag{1}$$

The pyroelectricity measurement shows that the antiferromagnetic arrangement between $\boldsymbol{S}_{\mathrm{Ni1}}$ and $\boldsymbol{S}_{\mathrm{Ni2}}$ enhances the polarization. Therefore, the coefficient C should be negative if the exchange striction is dominant. In the proposed weak ferromagnetic structure, as depicted in Fig. 5(e), the Ni1 and Ni2 moments can be represented by $\boldsymbol{S}_{\mathrm{Ni1}} = (S_x, S_y, 0)$ and $\boldsymbol{S}_{\mathrm{Ni2}} = (S_x, -S_y, 0)$, respectively, where x is the magnetic-field direction and y is set in the direction of the vector product of the c and x axes. The exchange striction is calculated to be $C(-S^2 + 2S_x^2)$, where S is the value of the Ni spin moment.

To calculate the contribution of the p-d hybridization mechanism to the electric polarization in a NiO_6 octahedral cluster with threefold rotational symmetry, we set six unit vectors $\boldsymbol{e}_{ij}^{\mathrm{NiO}}$ along the Ni-O bonds as

$$\boldsymbol{e}_{11}^{\mathrm{NiO}} = \begin{pmatrix} \sin\theta_1 \cos\phi_1 \\ \sin\theta_1 \sin\phi_1 \\ \cos\theta_1 \end{pmatrix}, \boldsymbol{e}_{12}^{\mathrm{NiO}} = \begin{pmatrix} \sin\theta_1 \cos\left(\phi_1 + \frac{2}{3}\pi\right) \\ \sin\theta_1 \sin\left(\phi_1 + \frac{2}{3}\pi\right) \\ \cos\theta_1 \end{pmatrix},$$
$$\boldsymbol{e}_{13}^{\mathrm{NiO}} = \begin{pmatrix} \sin\theta_1 \cos\left(\phi_1 - \frac{2}{3}\pi\right) \\ \sin\theta_1 \sin\left(\phi_1 - \frac{2}{3}\pi\right) \\ \cos\theta_1 \end{pmatrix}, \boldsymbol{e}_{21}^{\mathrm{NiO}} = \begin{pmatrix} \sin\theta_2 \cos\phi_2 \\ \sin\theta_2 \sin\phi_2 \\ \cos\theta_2 \end{pmatrix},$$
$$\boldsymbol{e}_{22}^{\mathrm{NiO}} = \begin{pmatrix} \sin\theta_2 \cos\left(\phi_2 + \frac{2}{3}\pi\right) \\ \sin\theta_2 \sin\left(\phi_2 + \frac{2}{3}\pi\right) \\ \cos\theta_2 \end{pmatrix},$$
$$\boldsymbol{e}_{23}^{\mathrm{NiO}} = \begin{pmatrix} \sin\theta_2 \cos\left(\phi_2 - \frac{2}{3}\pi\right) \\ \sin\theta_2 \sin\left(\phi_2 - \frac{2}{3}\pi\right) \\ \cos\theta_2 \end{pmatrix}, \tag{2}$$

where the index i denotes whether the oxygen positions are above ($i = 1$) or below ($i = 2$) Ni. The index j denotes the threefold symmetric Ni-O bonds in the c plane. The values of ϕ_1, ϕ_2, θ_1, and θ_2 are $65.9^\circ, 4.5^\circ, 48.7^\circ$, and 115.9° for the $Ni1O_6$ cluster and $1.5^\circ, 54.1^\circ, 49.2^\circ$, and 120.6° for the $Ni2O_6$ cluster, respectively [17]. The change in the electric polarization induced by the spin-direction dependent p-d hybridization mechanism ΔP_z^{pd} is given by

$$\begin{aligned} \Delta P_z^{pd} &\propto \sum_{i,j} \left(\boldsymbol{S}_{\mathrm{Ni}} \cdot \boldsymbol{e}_{ij}^{\mathrm{NiO}}\right)^2 e_{ijz}^{\mathrm{NiO}} \\ &= A\left(S_x^2 + S_y^2\right) + BS_z^2 \\ &= AS^2 + (B - A)S_z^2, \end{aligned} \tag{3}$$

where A and B are constants. This formula indicates that only the z component of the magnetic moment can affect P_z. The z component of magnetization thermally fluctuates around T_{C1}. The P_z value should change when the external magnetic field suppresses the fluctuation and modifies $\langle S_z^2 \rangle$. As shown in the P-H curves above T_{C2} in Figs. 4(b) and 4(d), we can determine that the sign of ΔP_z^{pd} is negative for both $\boldsymbol{H} \perp \boldsymbol{c}$ and $\boldsymbol{H} \parallel \boldsymbol{c}$; however, in magnetically ordered phases below T_{C1}, particularly at 4.2 K, that of ΔP_z^{ex} is negative for both $\boldsymbol{H} \parallel \boldsymbol{c}$ and $\boldsymbol{H} \perp \boldsymbol{c}$. The field dependence of electric polarization is shown in Fig. 4(b) at 70-90 K. At lower temperatures, the change in electric polarization appears to be dominated by the exchange striction mechanism because $S_z = 0$; thus, $\Delta P_z^{pd} \simeq 0$ in the field-induced weak ferromagnetic phase. In contrast, for $\boldsymbol{H} \parallel \boldsymbol{c}$, S_z is modified as H is increased; thus, $\Delta P_z^{pd} \neq 0$. The magnetization is approximately proportional to the field in each magnetic phase. Therefore, the electric polarization driven by the p-d hybridization should exhibit quadratic H dependence, as in the case of exchange striction, which is consistent with the experimental observation.

We further discuss whether the observed magnetic-field dependence of the electric polarization can be explained by the proposed soliton-phase scenario. In the soliton phase, S_x is increased and S_z decreased with increasing a magnetic field. Therefore, ΔP_z^{ex} is decreased according to Eq. (1) because the sign of C is negative. In contrast, ΔP_z^{pd} is increased according to Eq. (3) because the coupling constant of S_z is negative. These effects are canceled mutually. Consequently, the ME effect is approximately zero, as shown in Fig. 4(b). We consider that the proposed soliton phase is reasonable from the viewpoint of ME response.

IX. CONCLUSION

We observed giant pyroelectricity in Ni_2InSbO_6 driven by the helimagnetic order. When a magnetic field was applied in the $\boldsymbol{H} \perp \boldsymbol{c}$ configuration, a superlinear magnetization curve was observed. We interpret this magnetic property as 2π solitons that are created in the canted antiferromagnetic background assisted by the chiral polar nature of the system. The application of a magnetic field along the c axis triggered a metamagnetic transition with a hysteresis loop. It was also revealed that the magnetoelectric responses in each magnetic field configuration can be elucidated mainly by the exchange striction and p-d hybridization mechanisms. These particular magnetic and magnetoelectric properties may exist in similar low-symmetry antiferromagnetic helimagnets such as Ni_2ScSbO_6 [17] and $Fe_3PO_4O_3$ [24,25]. Further study is required on neutron scattering to determine the magnetic structure in each phase.

ACKNOWLEDGMENTS

This work was partly supported by the Japan Society for the Promotion of Science (JSPS) KAKENHI Grants No. JP25220803, No. JP16H01065, No. JP16K13828, No. JP19H01835, and No. JP19H05826. Y.A., T.S., and Y.F. are supported by the JSPS through the Program for Leading Graduate Schools (MERIT). The magnetization, electric polarization, x-ray reflection Laue photograph, and high-energy x-ray transmission Laue photograph were measured at the Institute for Solid State Physics (ISSP), University of Tokyo. The authors thank T. Yajima for assistance in the XRD experiment at the ISSP. The steady high magnetic field measurements were performed in the High Field Laboratory for Superconducting Materials, Institute for Materials Research, Tohoku University, Japan (Project No. 16H0023). The synchrotron soft x-ray measurements were performed under User Program No. 2015S2-007 at BL-16A and No. 2016PF-BL-19B at BL-19B, Photon Factory, KEK, Japan. The neutron scattering measurements were performed under User Program No. 2017A0069 at the Materials and Life Science Experimental Facilities, J-PARC, Japan. We would like to thank Editage (www.editage.com) for English language editing.

[1] I. Dzyaloshinsky, J. Phys. Chem. Solids **4**, 241 (1958).
[2] T. Moriya, Phys. Rev. **120**, 91 (1960).
[3] S. Mühlbauer, B. Binz, F. Jonietz, C. Pfleiderer, A. Rosch, A. Neubauer, R. Georgii, and P. Böni, Science **323**, 915 (2009).
[4] Y. Tokunaga, X. Yu, J. White, H. M. Rønnow, D. Morikawa, Y. Taguchi, and Y. Tokura, Nat. Commun. **6**, 7638 (2015).
[5] S. Seki, X. Yu, S. Ishiwata, and Y. Tokura, Science **336**, 198 (2012).
[6] I. Kézsmárki, S. Bordács, P. Milde, E. Neuber, L. Eng, J. White, H. M. Rønnow, C. Dewhurst, M. Mochizuki, K. Yanai *et al.*, Nat. Mater. **14**, 1116 (2015).
[7] Y. Fujima, N. Abe, Y. Tokunaga, and T. Arima, Phys. Rev. B **95**, 180410(R) (2017).
[8] T. Kurumaji, T. Nakajima, V. Ukleev, A. Feoktystov, T. H. Arima, K. Kakurai, and Y. Tokura, Phys. Rev. Lett. **119**, 237201 (2017).
[9] A. K. Nayak, V. Kumar, T. Ma, P. Werner, E. Pippel, R. Sahoo, F. Damay, U. K. Rößler, C. Felser, and S. S. Parkin, Nature (London) **548**, 561 (2017).
[10] S. Seki, S. Ishiwata, and Y. Tokura, Phys. Rev. B **86**, 060403(R) (2012).
[11] E. Ruff, S. Widmann, P. Lunkenheimer, V. Tsurkan, S. Bordács, I. Kézsmárki, and A. Loidl, Sci. Adv. **1**, e1500916 (2015).
[12] G.-H. Cai, M. Greenblatt, and M.-R. Li, Chem. Mater. **29**, 5447 (2017).
[13] I. Živković, K. Prša, O. Zaharko, and H. Berger, J. Phys.: Condens. Matter **22**, 056002 (2010).
[14] Y. S. Oh, S. Artyukhin, J. J. Yang, V. Zapf, J. W. Kim, D. Vanderbilt, and S.-W. Cheong, Nat. Commun. **5**, 3201 (2014).
[15] J. W. Kim, S. Artyukhin, E. D. Mun, M. Jaime, N. Harrison, A. Hansen, J. J. Yang, Y. S. Oh, D. Vanderbilt, V. S. Zapf *et al.*, Phys. Rev. Lett. **115**, 137201 (2015).
[16] M. O. Yokosuk, A. al-Wahish, S. Artyukhin, K. R. O'Neal, D. Mazumdar, P. Chen, J. Yang, Y. S. Oh, S. A. McGill, K. Haule, S.-W. Cheong, D. Vanderbilt, and J. L. Musfeldt, Phys. Rev. Lett. **117**, 147402 (2016).
[17] S. A. Ivanov, R. Mathieu, P. Nordblad, R. Tellgren, C. Ritter, E. Politova, G. Kaleva, A. Mosunov, S. Stefanovich, and M. Weil, Chem. Mater. **25**, 935 (2013).
[18] S. Quezel, F. Tcheou, J. Rossat-Mignod, G. Quezel, and E. Roudaut, Physica B+ C **86-88**, 916 (1977).
[19] R. Kajimoto, H. Yoshizawa, H. Shintani, T. Kimura, and Y. Tokura, Phys. Rev. B **70**, 012401 (2004).
[20] P. Day, A. Dinsdale, E. Krausz, and D. Robbins, J. Phys. C **9**, 2481 (1976).
[21] P. Day and K. Ziebeck, J. Phys. C **13**, L523 (1980).
[22] A. Adam, D. Billerey, C. Terrier, R. Mainard, L. Regnault, J. Rossat-Mignod, and P. Meriel, Solid State Commun. **35**, 1 (1980).
[23] T. Adams, A. Chacon, M. Wagner, A. Bauer, G. Brandl, B. Pedersen, H. Berger, P. Lemmens, and C. Pfleiderer, Phys. Rev. Lett. **108**, 237204 (2012).
[24] K. A. Ross, M. M. Bordelon, G. Terho, and J. R. Neilson, Phys. Rev. B **92**, 134419 (2015).

[25] C. Sarkis, M. J. Tarne, J. R. Neilson, H. B. Cao, E. Coldren, M. P. Gelfand, and K. A. Ross, Phys. Rev. B **101**, 184417 (2020).
[26] A. Bogdanov and D. Yablonskii, Zh. Eksp. Teor. Fiz. **95**, 182 (1989).
[27] A. Zheludev, G. Shirane, Y. Sasago, N. Koide, and K. Uchinokura, Phys. Rev. B **54**, 15163 (1996).
[28] A. Zheludev, S. Maslov, G. Shirane, Y. Sasago, N. Koide, and K. Uchinokura, Phys. Rev. B **57**, 2968 (1998).
[29] S. Mühlbauer, S. N. Gvasaliya, E. Pomjakushina, and A. Zheludev, Phys. Rev. B **84**, 180406(R) (2011).
[30] S. Mühlbauer, S. Gvasaliya, E. Ressouche, E. Pomjakushina, and A. Zheludev, Phys. Rev. B **86**, 024417 (2012).
[31] J. Chovan, N. Papanicolaou, and S. Komineas, Phys. Rev. B **65**, 064433 (2002).
[32] J. Chovan, M. Marder, and N. Papanicolaou, Phys. Rev. B **88**, 064421 (2013).
[33] M. Janoschek, P. Fischer, J. Schefer, B. Roessli, V. Pomjakushin, M. Meven, V. Petricek, G. Petrakovskii, and L. Bezmaternikh, Phys. Rev. B **81**, 094429 (2010).
[34] Y. Ichiraku, R. Takeda, S. Shimono, M. Mito, Y. Kubota, K. Inoue, and Y. Kato, J. Phys. Soc. Jpn. **88**, 094710 (2019).
[35] X. Zhang, Y. Zhou, and M. Ezawa, Sci. Rep. **6**, 24795 (2016).
[36] X. Zhang, Y. Zhou, and M. Ezawa, Nat. Commun. **7**, 10293 (2016).
[37] P. F. Bessarab, D. Yudin, D. R. Gulevich, P. Wadley, M. Titov, and O. A. Tretiakov, Phys. Rev. B **99**, 140411(R) (2019).
[38] W. Legrand, D. Maccariello, F. Ajejas, S. Collin, A. Vecchiola, K. Bouzehouane, N. Reyren, V. Cros, and A. Fert, Nat. Mater. **19**, 34 (2020).
[39] T. Kimura, T. Goto, H. Shintani, K. Ishizaka, T. Arima, and Y. Tokura, Nature (London) **426**, 55 (2003).
[40] M. Weil, R. Mathieu, P. Nordblad, and S. Ivanov, Cryst. Res. Technol. **49**, 142 (2014).
[41] M. A. Prosnikov, A. N. Smirnov, V. Y. Davydov, Y. Araki, T. Arima, and R. V. Pisarev, Phys. Rev. B **100**, 144417 (2019).
[42] X. Wang, F.-T. Huang, J. Yang, Y. S. Oh, and S.-W. Cheong, APL Mater. **3**, 076105 (2015).
[43] Y. Yamasaki, T. Sudayama, J. Okamoto, H. Nakao, M. Kubota, and Y. Murakami, J. Phys.: Conf. Ser. **425**, 132012 (2013).
[44] Y. Yamasaki, D. Morikawa, T. Honda, H. Nakao, Y. Murakami, N. Kanazawa, M. Kawasaki, T. Arima, and Y. Tokura, Phys. Rev. B **92**, 220421(R) (2015).
[45] S.-i. Takata, J.-i. Suzuki, T. Shinohara, T. Oku, T. Tominaga, K. Ohishi, H. Iwase, T. Nakatani, Y. Inamura, T. Ito *et al.*, JPS Conf. Proc. **8**, 036020 (2015).
[46] Y. Tokura, S. Seki, and N. Nagaosa, Rep. Prog. Phys. **77**, 076501 (2014).
[47] L. J. Bannenberg, K. Kakurai, P. Falus, E. Lelièvre-Berna, R. Dalgliesh, C. D. Dewhurst, F. Qian, Y. Onose, Y. Endoh, Y. Tokura *et al.*, Phys. Rev. B **95**, 144433 (2017).
[48] J. S. White, A. Butykai, R. Cubitt, D. Honecker, C. D. Dewhurst, L. F. Kiss, V. Tsurkan, and S. Bordács, Phys. Rev. B **97**, 020401(R) (2018).
[49] Y. Togawa, T. Koyama, K. Takayanagi, S. Mori, Y. Kousaka, J. Akimitsu, S. Nishihara, K. Inoue, A. Ovchinnikov, and J.-i. Kishine, Phys. Rev. Lett. **108**, 107202 (2012).
[50] C. Pappas, Physics **5**, 28 (2012).
[51] Y. Togawa, Y. Kousaka, K. Inoue, and J.-i. Kishine, J. Phys. Soc. Jpn. **85**, 112001 (2016).
[52] T. Nagamiya, K. Nagata, and Y. Kitano, Prog. Theor. Phys. **27**, 1253 (1962).
[53] T. Nagamiya, *Solid State Physics* (Elsevier, Amsterdam, 1968), Vol. 20, pp. 305–411.
[54] Y. A. Izyumov, Sov. Phys. Usp. **27**, 845 (1984).
[55] C. Ederer and N. A. Spaldin, Phys. Rev. B **71**, 060401(R) (2005).
[56] M. Tokunaga, M. Akaki, T. Ito, S. Miyahara, A. Miyake, H. Kuwahara, and N. Furukawa, Nat. Commun. **6**, 5878 (2015).
[57] J. Lass, C. R. Andersen, H. K. Leerberg, S. Birkemose, S. Toth, U. Stuhr, M. Bartkowiak, C. Niedermayer, Z. Lu, R. Toft-Petersen *et al.*, Phys. Rev. B **101**, 054415 (2020).
[58] K.-L. Ji, E. Solana, A. M. A. Lopez, P. Manuel, C. Ritter, A. Senyshyn, and P. Attfield, Chem. Commun. **54**, 12523 (2018).
[59] H. Katsura, N. Nagaosa, and A. V. Balatsky, Phys. Rev. Lett. **95**, 057205 (2005).
[60] T. Arima, J. Phys. Soc. Jpn. **76**, 073702 (2007).